Journal of Power Sources 478 (2020) 229026

Contents lists available at ScienceDirect

Journal of Power Sources

journal homepage: www.elsevier.com/locate/jpowsour

Theory of battery ageing in a lithium-ion battery: Capacity fade, nonlinear ageing and lifetime prediction

Selcuk Atalay [a,*], Muhammad Sheikh [a], Alessandro Mariani [b], Yu Merla [d], Ed Bower [c], W. Dhammika Widanage [a,**]

[a] WMG, University of Warwick, Coventry, CV4 7AL, UK
[b] Fiat Powertrain Technologies Industrial, Arbon, CH-9320, Switzerland
[c] Aston Martin Lagonda, Warwickshire, CV35 9JY, UK
[d] Williams Advanced Engineering, Grove, Oxfordshire, OX12 0DQ, UK

HIGHLIGHTS

- A battery model capable of predicting SEI and Li plating induced aging is developed.
- Mass transport of EC and DMC molecules within anode is considered.
- The model predicts the lifetime based on actual drive-profiles with fast charging.
- The importance of multi-layered SEI and its effect on porosity change is explained.
- The model is able to capture the transition from linear to nonlinear aging.

GRAPHICAL ABSTRACT

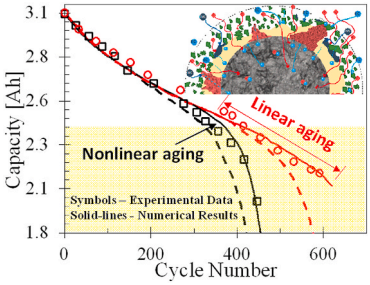

ARTICLE INFO

Keywords:
Battery ageing
Capacity fade
Nonlinear aging
Drive-cycle life
Lifetime prediction
Lithium-ion battery

ABSTRACT

Forecasting the lifetime of Li-ion batteries is a critical challenge that limits the integration of battery electric vehicles (BEVs) into the automotive market. Cycle-life performance of Li-ion batteries is intrinsically linked to the fundamental understanding of ageing mechanisms. In contrast to most previous studies which utilise empirical trends (low real-time information) or rough simplifications on mathematical models to predict the lifetime of a Li-ion battery, we deployed a novel ageing formulation that includes heterogeneous dual-layer solid electrolyte interphase (SEI) and lithium-plating ageing mechanisms with porosity evaluation. The proposed model is parameterized and optimized for mass transport and ageing parameters based on fresh and an aged cell and validated against our experimental results. We show that our advanced ageing mechanisms can accurately calculate experimentally observed cell voltage and capacity fade with respect to cycling number and can predict future fade for new operating scenarios based on constant-current and a dynamic power profile cycling experimental data consisting of high discharge C-rates and fast-charging periods. Our model is able to capture the linear and nonlinear (knee-point) capacity fade characteristics with a high accuracy of 98% goodness-of-fit-error and we compared our model performance with well-accepted existing model in literature.

* Corresponding author.
** Corresponding author.
E-mail addresses: selcukatalay.batteryscientist@gmail.com (S. Atalay), dhammika.widanalage@warwick.ac.uk (W.D. Widanage).

https://doi.org/10.1016/j.jpowsour.2020.229026
Received 24 June 2020; Received in revised form 2 September 2020; Accepted 28 September 2020
Available online 14 October 2020
0378-7753/

1. Introduction

The study of lithium (Li)-ion batteries is currently of huge scientific and technological interest in order to reduce fossil energy powered automobiles in the market. Hence, the automobile manufacturers are encouraged to push towards electrification. There are several major barriers for achieving a strong competitor role in the electrification market; maximum range, fast-charging ability, lifetime and safety are the key performance elements whilst a customer decides on purchasing an electric vehicle (EV) [1,2]. These key elements can be profoundly influenced by the battery degradation mechanism, which causes capacity loss and resistance increase over the lifetime [3]. Battery degradation can be a serious problem in the automotive industry affecting the vehicles warranty period and compromise an industry's reputation in the business market role [4]. Hence fundamental understanding of degradation mechanisms is critical for the development of reliable life-prediction methods for battery management systems (BMS).

Identifying ageing mechanism in a Li-ion battery is the main and most challenging goal, therefore a wide range of experimental and simulation approaches have provided considerable insight into the battery degradation that causes capacity loss [3,5–7]. Post-mortem analysis methods; such as X-ray photoelectron spectroscopy (XPS) [8], X-ray diffraction (XRD) [9,10], scanning electron microscopy (SEM) [4,11,12], and electrochemical impedance spectroscopy (EIS) [12] techniques, have yielded refined indications for morphological changes of the electrodes, the electrolyte, the separator, and the current collectors over lifetime period [13]. Although, there is no significant morphological modification reported for the positive electrode [14–16], a common theme emerging from these studies is that solid electrolyte interphase (SEI) [7,13,15,17] and deposition of metallic lithium in the anode (lithium-plating) [15,18], causes substantial cell ageing [7,15,17,18]. Similar depositions of at the cathode, termed as cathode electrolyte interphase from electrolyte oxidation, has been reported [19]. However these side reactions can generate gaseous compounds (such as hydrogen and hydrogen fluoride) and is not considered as the primary ageing mechanism in this study.

As many studies have already showed that formation of SEI and lithium-plating passive film layers at the anode electrode are formed by consuming of the cyclable Li-ions [7,17] and can extend hundreds of nanometers in thickness [7,20]. This large non-homogeneous morphological passive films growth on active material geometry causes; (i) drastic decrease in electrode porosity and (ii) limits the kinetic transport of lithium-ions through those inactive areas and causes resistance increase and capacity fade [18]. Despite many existing ageing models showing a good comparison against experimental studies, the models consider SEI composed of a homogeneous layer with the assumption of linear solvent diffusion in the SEI with a constant base reaction rate and SEI growth. The layer is treated as a non-porous block with a sharp interphase and the effect of film growth on the anode electrode volume is ignored [17,18,21–26], although the recent experimental studies show that these passive film formation has multi-layered structure of SEI with a dense layer of inorganic components close to graphite electrode followed by a porous organic layer close to electrolyte [7,13,27]. The nanoporous structure of SEI influence Li-ion mass transport and also kinetics as theoretical studies show that diffusion within a porous structure hinders the diffusion coefficient and causes a lack of communication of Li-ion with active material [28]. Since the performance of the battery is highly coupled with the effective diffusion coefficient of Li-ion, quantifying all these ageing features precisely will improve lifetime prediction of cell capacity during cell operation.

The objective of this study is to investigate the lifetime of a NCA/graphite Li-ion cell at a constant-current (CC) and dynamic power profile at 25 °C by deploying a well-known P2D battery model with our novel ageing mechanism of multi-layered heterogeneous SEI growth and lithium-plating and coupling the diffusion coefficients of Li-ion, EC and DMC as a function of local porosity. The experimentally measured capacity fade and terminal voltage of the cell during cycling are compared against the model and captured linear and nonlinear capacity fades at high and low C-rates, respectively. For the first time, the model is employed to predict the lifetime of a cell for a dynamic power profile and estimated the future capacity fade despite a limited availability of measured capacity data.

1.1. 2- Experimental measurements

To evaluate ageing, several parameters are considered including capacity fade and resistance increase, which indicates the cell State-of-Health (SOH). SoH is important to predict remaining useful life. The capacity is a key performance indicator for high-energy applications such as electric vehicles where it can be considered one of the key criteria for end-of-life (EoL) prediction when the capacity reaches 70% of its initial value. Cells used for this study are high-power cylindrical lithium-ion cells. The cell has dimensions of 18 mm diameter and 65 mm length. In this work, Maccor cyclers are used and fully oil immersed test rig was designed where we used dielectric oil (kryo-51) for safety and improved cell thermal management. As a further safety precaution, the rig was also placed in an environmental chamber. Cell connections are voltage sense cables and cycler channels are connected on brass blocks to record current and voltage data. For individual cell's temperature measurements thermocouples are connected which then assigned to relevant Maccor channels to record temperature change during live tests. Test rig placed in the thermal chamber, which has additional safety systems including air-cooling and temperature distribution to control and maintain cell temperature at desire level.

Two test conditions are considered, where the first experiment is used for cell cycling using a constant current (CC) step of C/3 to a cut-off voltage of 4.2 V, followed by a constant voltage (CV) step at 4.2 V until the charge current dropped to 0.1 A. Following to 1 min rest period, the cell was discharged with either a constant current of 1C–2.5 V for the 1C discharge cycle or a discharge current of 4C to 2.5 V for the 4C discharge cycle followed by the 1 min rest before the next charge step. 30 cycles for 1C discharge and 40 cycles for 4C discharge were performed before reference performance test (RPT) at 25 °C to determine the cell capacity. For each cycling test (1C and 4C) three cells were used and the cells were cycled until they reach 70% of its initial capacity, at which point the cells were deemed to have reached EoL and the experiment ended.

In the second test condition a dynamic power profile is designed to utilise a higher depth-of-discharge (97%–23%) with one fast charge event (8.5 [W]) and two slow charge events (3.75 [W]) per cycle as shown in Fig. 4a. The dynamic power cycle is to emulate realistic driving user cases and support industry warranty decisions, for which a CCCV profile is not ideal. Each warranty cycle took 15 h and a RPT capacity check was done after five warranty cycles. The RPT capacity test included a CC-CV regime with a CC step of 1C to a cut-off voltage of 4.2 V, followed by a constant voltage (CV) step at 4.2 V until the charge current dropped to 0.1 A. Following a1 hour rest period the cell was then discharged at a constant current of C/3 to 2.5 V to get the reference capacity value of the cell. Data is recorded with a 1 s sampling time and thermocouple control is used to bring back temperature at 25 °C after charge and discharge steps.

1.2. 3- Mathematical model

We considered a commercial lithium-ion cell which consists of current collectors at the both ends, the negative electrode, the separator and the positive electrode domains as schematically shown in Fig. 1a. A binary electrolyte is considered to fill the porous components of electrodes.

The electrochemical model used in this work incorporated with multi-layered SEI and lithium plating is based on the pseudo two-dimensional model (P2D) which was described in Ref. [29]. In the present study, the model is developed to analyse the behaviour of critical

ageing mechanisms and their impact on capacity fade in a lithium-ion cell. The model ignores the heat generation due to Ohmic resistance in this work. The full governing equations and appropriate boundary conditions are listed in the Supplementary Information.

There are 5 main electrochemical reactions considered that occur at the anode electrode domain as illustrated in Fig. 1b:

$$C_6 + Li^+ + e^- \leftrightarrow LiC_6 \tag{1}$$

Eq. (1) is the intercalation reaction that occurs in the active material graphite surface. For the lithium intercalation reaction in cathode and anode, the local current density per active material area is calculated by the Butler-Volmer equation:

$$j_{int} = i_{0,int}\left(exp\left(\eta_{int}\frac{\alpha_{a,int}F}{RT}\right) - exp\left(\eta_{int}\frac{\alpha_{c,int}F}{RT}\right)\right) \tag{2}$$

where $i_{0,int}$ is the exchange current density of lithium intercalation, $\alpha_{a,int}$ and $\alpha_{c,int}$ are the anodic and cathodic charge transfer coefficients, respectively, and η_{int} is the surface overpotential defined as:

$$\eta_{int} = \varphi_s - \varphi_e - U_{eq}^{int} - j_{total}R_{film} \tag{3}$$

where φ_s and φ_e are electric potentials in the solid and electrolyte phases. U_{eq}^{int} is the equilibrium potential for lithium intercalation reaction, F is Faraday constant and R_{film} is the resistance of the surface film due to the side reactions.

1.3. Ageing mechanism

$$Li^+ + e^- \leftrightarrow Li_{(s)} \tag{4}$$

The lithium deposition reaction Eq. (4) is considered as one of the side reactions on graphite. $Li_{(s)}$ is the product of metallic lithium deposited on the graphite surface, Eq. (4) competes with the intercalation reaction (Eq. (1)) when the lithium deposition potential (LDP) gets below zero, $Li^+/Li(\eta_{Li^+/Li} < 0)$. Due to charge transfer limitations, lithium ions are inclined to deposit instead of intercalating into the negative electrode. The lithium plating is assumed to be irreversible in the model, which implies stripping of plated lithium is neglected and the lithium-plating current density is described as following:

$$j_{plating} = -i_0^{plating}\left[exp\left(-\frac{\alpha_c^{plating}F}{RT}\left(\varphi_s - \varphi_e - j_{total}R_{film} - U_{eq}^{plating}\right)\right)\right] \tag{5}$$

where $i_0^{plating}$ is the exchange current density of lithium plating which is considered as a fitting parameter due to the lack of reliable experimental data and $U_{eq}^{plating}$ considered as zero in the present work.

The second ageing mechanism, SEI growth, is governed by two electrochemical reactions as follows:

$$2Li^+ + 2(C_3H_4O_3)(EC) + 2e^- \leftrightarrow (CH_2OCO_2Li)_2 + C_2H_4 \tag{6}$$

$$2Li^+ + C_3H_6O_3(DMC) + 2e^- \leftrightarrow Li_2CO_3 + C_2H_6 \tag{7}$$

The products, $(CH_2OCO_2Li)_2$ and Li_2CO_3, are the main inorganic components of solid electrolyte interphase (SEI) multilayers. The releasing flammable hydrocarbon gases, such as ethane and methane are ignored in this work for simplicity. The rate of SEI formation reaction is affected by the mass transport of EC and DMC within the anode and by the surface kinetics. The local current densities of the SEI formation reaction is calculated by the cathodic BV expressions below:

$$j_{SEI}^{total} = j_{SEI}^{EC} + j_{SEI}^{DMC} \tag{8}$$

$$j_{SEI}^{EC} = -Fk_0^{EC}c_{EC}^s\left[exp\left(-\frac{\alpha_{c,EC}F}{RT}\left(\varphi_s - \varphi_e - j_{total}R_{film} - U_{SEI}^{EC}\right)\right)\right] \tag{9}$$

$$j_{SEI}^{DMC} = -Fk_0^{DMC}c_{DMC}^s\left[exp\left(-\frac{\alpha_{c,DMC}F}{RT}\left(\varphi_s - \varphi_e - j_{total}R_{film} - U_{SEI}^{DMC}\right)\right)\right] \tag{10}$$

where k_0^{EC} and k_0^{DMC} are the kinetic rate constants for EC and DMC; U_{SEI}^{EC} and U_{SEI}^{DMC} are the equilibrium potentials of SEI for EC and DMC, and c_{EC}^s and c_{DMC}^s are the concentrations of EC and DMC on the surface of graphite, which is calculated based on the Fick's Law:

$$\frac{\partial(\varepsilon_e c_i)}{\partial t} - D_i^{eff}\nabla^2 c_i = j_{total} \tag{11}$$

where ε_e is volume fraction of the electrolyte, and it is calculated by $\varepsilon_e = 1 - \varepsilon_p - \varepsilon_{carbon}$. ε_p, and ε_{carbon} are active material and carbon-binder volume fractions in the anode porous electrode, respectively. ε_p is a quantity depending on the time and position as calculated in Eq. (20). D_i^{eff} is the diffusion coefficients of species EC and DMC and it is a function of SEI porosity (as described in the following section), c_i is the concentration of species EC and DMC in the anode electrolyte. The bulk electrolyte amount is consumed due to the side reactions deposited on the electrode particles as described in Eqs. (5), (9) and (10) and hence its volume fraction changes. The effective diffusion coefficient and effective electrolyte conductivity values are calculated based on the Bruggeman relation as following:

$$D_i^{eff} = \varepsilon_{SEI}^{\beta}D_i^0 \tag{12}$$

$$\kappa_i^{eff} = \varepsilon_{SEI}^{1.5}\kappa_i^0 \tag{13}$$

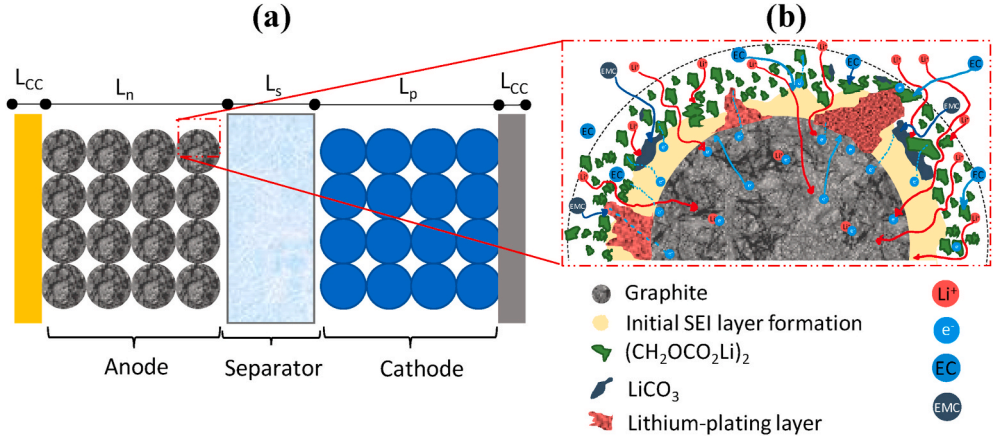

Fig. 1. (a) Schematic illustration of the 1D simulation domain and its 2D representation (b) Side reaction products (ageing mechanism) on anode active material.

Table 1
Physicochemical model geometry and electrochemical parameters measured and estimated from experimental data. Superscript *m* indicates measured values and *o* optimized values.

Parameter	Anode	Separator	Cathode
Geometry			
Thickness, l	55μmm	12 μmm	47.5μmm
Solid phase fraction, ε_s	0.42		0.48
Liquid phase fraction, ε_l	0.44	0.4	0.44
Particle radius, R_s	10.7°μm		17.5°μm
Thermodynamics			
Equilibrium voltage, E_{Eq}	see Fig. S1 (a)		see Fig. S1 (b)
Maximum Li + concentration, $c_{s,max}$	31,363 mol m^{-3} o		56,435 mol m^{-3} o
Kinetics			
Reaction rate constant, k_{ref}	1 × 10^{-11} ms^{-1} o		1 × 10-11 ms^{-1} o
Anodic charge-transfer coefficient, $\alpha_{a,init}$	0.5		0.5
Cathodic charge-transfer coefficient, $\alpha_{c,init}$	0.5		0.5
Exchange current density, $i_{0,int}$	13.2 × 10^4 Am-2 o		6.79 × 10^4 Am^{-2} o
Transport			
Solid diffusivity, D_s	3.9 × 10–14 m^2 s^{-1} [23]		8 × 10^{-14} m^2s^{-1} [23]
Solid conductivity, σ	100 S m^{-1} [23]		2 S m^{-1} [23]
Parameter		**Electrolyte**	
Electrolyte concentration, c_l		1000 mol m^{-3}	
Electrolyte diffusion, D_l		2.6 × 10^{-6} m^2s^{-1}	
Electrolyte conductivity, κ		$1106c_e\exp(-8900c_e^{1.4})$	
Transport number, t_+		0.38 [26]	

D_i^{eff} is calculated by Eq. (12) and D_i^0 is bulk diffusion coefficient of Li and $\varepsilon_{SEI}^{\beta}$ is the local porosity of the SEI layer and β represents the difficulty of electrolyte transport through the SEI layer and it is specified as around 20 [30]. κ_i^{eff} is the effective electronic conductivity with κ_i^0 bulk conductivity for all SEI compounds. The change in concentration of species of Li and c_{SEI}^{EC}, and c_{SEI}^{DMC} layers are calculated as an equivalent thickness of the surface film by the Faraday's law as following:

$$\frac{\partial c_{SEI}^{EC}}{\partial t} = -\frac{j_{SEI}^{EC}}{2F} \tag{14}$$

$$\frac{\partial c_{SEI}^{DMC}}{\partial t} = -\frac{j_{SEI}^{DMC}}{2F} \tag{15}$$

$$\frac{\partial c_{Li}}{\partial t} = -\frac{j_{Li}}{F} \tag{16}$$

Finally, the total reaction rate (j_{total}), can be summed as; (i) main reaction rate (j_{int}), (ii) SEI formation reactions (j_{SEI}^{total}), and (iii) lithium deposition reaction rate ($j_{plating}$). All of intercalation, lithium deposition reaction rates and SEI formations can be described using Butler-Volmer (BV) equation, as presented in Eqs. (2), (5) and (8), respectively.

$$j_{total} = j_{int} + j_{SEI}^{total} + j_{plating} \tag{17}$$

1.4. Surface film: thickness, film resistance and particle sphere geometries

SEI layers and lithium plating constitute the surface film covering graphite particles. In the model, graphite particles are assumed to be spherical and the surface film is assumed to be non-uniform in thickness along the anode electrode. As such, the amount of SEI and lithium plating can be transformed to an equivalent thickness of the surface film, as:

$$\delta_{film}(x,t) = \frac{1}{a_s(x,t)}\left(\frac{c_{SEI}^{EC}M_{SEI}^{EC}}{\rho_{SEI}^{EC}} + \frac{c_{SEI}^{DMC}M_{SEI}^{DMC}}{\rho_{SEI}^{DMC}} + \frac{c_{Li}M_{Li}}{\rho_{Li}}\right) \tag{18}$$

where $a_s(x,t)$, M_i and ρ_i are active material particle surface area, molar weights and densities for species, respectively. The ratio of the molar weights to the density corresponds to a specific volume for each of species formed on graphite electrodes and they are given as molar volume ($\overline{V}_i^j$) in Table 2. The resistance of surface films in Eq. (19) is determined with the contribution of 3 species as following:

$$R_{film}(x,t) = \varepsilon_{SEI}^{(CH_2OCO_2Li)_2}\frac{\delta_{film}^{(CH_2OCO_2Li)_2}}{\kappa_{SEI}^{(CH_2OCO_2Li)_2}} + \varepsilon_{SEI}^{Li_2CO_3}\frac{\delta_{film}^{Li_2CO_3}}{\kappa_{SEI}^{Li_2CO_3}} + \varepsilon_{Li}\frac{\delta_{film}^{Li}}{\kappa_{Li}} \tag{19}$$

where $\varepsilon_{SEI}^{(CH_2OCO_2Li)_2}$, $\varepsilon_{SEI}^{Li_2CO_3}$, and ε_{Li} are the volume fraction of $(CH_2OCO_2Li)_2$, Li_2CO_3 and lithium-plating in the film, respectively and $\kappa_{SEI}^{(CH_2OCO_2Li)_2}$, $\kappa_{SEI}^{Li_2CO_3}$, and κ_{Li} are the ionic conductivity of $(CH_2OCO_2Li)_2$,

Table 2
Parameters for the side reaction definitions. The superscript *o* in the values indicates optimized values.

Symbol	Parameter	Value
SEI Layers		
$E_{Eq,SEI}$	SEI formation equilibrium potential	0.4 V [30]
κ_{SEI}	Li^+ conductivity	1 × 10^{-2} S m^{-1}
σ_{SEI}	e^- conductivity	1 × 10^{-8} S m^{-1}
U_{SEI}^{DMC}	DMC reduction potential	0.3 V
$D^0{}_{DMC}$	DMC diffusion coefficient	10^{-6} cm^2 s^{-1o}
k_{DMC}^0	DMC reaction rate	1.8 × 10^{-8} m s^{-1o}
c_{DMC}^o	DMC concentration in bulk electrolyte	4.5 mol L^{-1}
$\overline{V}_{SEI}^{Li_2CO_3}\rho_{SEI,}$	Molar volume of Li_2CO_3	84.2 cm^3 mol^{-1o}
$\varepsilon_{SEI}^{Li_2CO_3}$	Volume fraction of Li_2CO_3	0.05 [26]
U_{SEI}^{EC}	EC reduction potential	0.8 V
$D^0{}_{EC}$	EC diffusion coefficient	10^{-6} cm^2 s^{-1o}
k_{EC}^0	EC reaction rate	0.8 × 10^{-8} m s^{-1}
c_{EC}^o	EC concentration in bulk electrolyte	4.5 mol L^{-1}
$\overline{V}_{SEI}^{(CH_2OCO_2Li)_2}$	Molar volume of $(CH_2OCO_2Li)_2$	66.7 cm^3 mol^{-1o}
$\varepsilon_{SEI}^{(CH_2OCO_2Li)_2}$	Volume fraction of $(CH_2OCO_2Li)_2$	0.03 [26]
Lithium-Plating		
$U_{eq}^{plating}$	Plating equilibrium potential	0.0 V
$i_{0,plating}$	Plating exchange current density	6.05 × 10^{-6} A m^{-2o}
ρ_{Li}	Density of Li-plating	2110 kg m^{-3o}
M_{Li}	Molar mass of Li-plating	73.889 g mol^{-1o}
ε_{Li}	Volume fraction of Li-plating	0.76

Table 3
Governing equations and boundary conditions for positive and negative electrodes in a pseudo two-dimensional model (x and r).

Governing Equations	Boundary Conditions	
	Negative Electrode	Positive Electrode
Mass balance in the electrolyte for a binary salt concentrated electrolyte		
$\frac{\partial(\varepsilon_e c_e)}{\partial t} = D_{eff,e}\frac{\partial^2 c_e}{\partial x^2} + \frac{(1-t_+^0)j_{int}}{F}$ with initial condition of $c_e\|_{t=0} = c_0$	$-D_{eff,n}\frac{\partial c_e}{\partial x}\|_{x=0} = 0$ $-D_{eff,n}\frac{\partial c_e}{\partial x}\|_{x=L_{n^-}} = -D_s\frac{\partial c_e}{\partial x}\|_{x=L_{n^+}}$	$-D_{eff,p}\frac{\partial c_e}{\partial x}\|_{x=L_n+L_s+L_p} = 0$ $-D_s\frac{\partial c_e}{\partial x}\|_{x=L_{n^-}+L_s} = -D_{eff,n}\frac{\partial c_e}{\partial x}\|_{x=L_{n^+}+L_s}$
Electric potential distribution in solution		
$\nabla\left(-\kappa_{eff,m}\frac{\partial\varphi_e}{\partial x} + \frac{2\kappa_{eff,m}RT}{F}(1-t_+^0)\frac{\partial(\ln c_e)}{\partial x}\right) = j_{int}$	$-\kappa_{eff,n}\frac{\partial\varphi_s}{\partial x}\|_{x=0} = 0$ $-\kappa_{eff,n}\frac{\partial\varphi_s}{\partial x}\|_{x=L_{n^-}} = -\kappa_s\frac{\partial\varphi_s}{\partial x}\|_{x=L_{n^+}}$	$-\kappa_{eff,p}\frac{\partial\varphi_s}{\partial x}\|_{x=L_n+L_s+L_p} = 0$ $-\kappa_s\frac{\partial\varphi_s}{\partial x}\|_{x=L_{n^-}+L_s} = -\kappa_{eff,p}\frac{\partial\varphi_s}{\partial x}\|_{x=L_{n^+}+L_s}$
Electric potential distribution in matrix/solid phase		
$\frac{\partial(\sigma_{eff,m}\varphi_s)}{\partial x^2} = Fj_m$	$\frac{\partial\varphi_s}{\partial x}\|_{x=L_n+L_s} = 0$ $-\sigma_{eff,n}\frac{\partial\varphi_s}{\partial x}\|_{x=L_n} = 0$	$-\varphi_s\|_{x=0} = 0$ $\frac{\partial\varphi_s}{\partial x}\|_{x=L_n+L_s+L_p} = -\frac{I_{app}}{\sigma_{eff,p}}$
Mass balance in the electrodes in the matrix/solid phase		
$\frac{\partial c_s}{\partial t} = \frac{1}{r^2}\frac{\partial}{\partial r}\left(D_m r^2\frac{\partial c_s}{\partial r}\right)$ with the initial conditions of $c_s\|_{t=0} = c_s^0$	$\frac{\partial c_s}{\partial r}\|_{r=0} = 0$	$-D_m\frac{\partial c_s}{\partial r}\|_{r=R_p} = j_m$

* m is either n or p depending on the material type.

Li_2CO_3 and lithium plating, respectively.

The porosity of the anode active material in the present work evolves with the surface film formed due to SEI and lithium plating as shown in Eq. (19). The volume fraction of the anode electrode increases with the growth of film and that of the electrolyte is reduced via the following expression:

$$\frac{d\varepsilon_p(x,t)}{dt} = a_s(x,t)\frac{d\delta_{film}(x,t)}{dt} \tag{20}$$

where ε_p is the volume fraction of anode active material. As mentioned above one feature of the present model is that the diffusion coefficient of lithium ions in the porous medium is a function of the volume fraction porosity and Eqs. (12) and (13) are updated based on the calculated new porosity value in Eq. (20). It is also worth mentioning that $a_s(x,t)$ in Eq. (20) updates itself for each time step taken by the solver and in electrode thickness based on the determined new film thickness from Eq. (18).

2. Results and discussion

The presented 1D pseudo two-dimensional (P2D) battery model is numerically solved by a commercial finite element package, COMSOL Multiphysics (version 5.5), operated in a high-performance workstation. The computational domain is discretised into elements and finer node points on the boundaries of anode/separator domains is adopted to capture the side-reactions. The governing equations and appropriate boundary conditions are listed in Table 3 and Table 4.

2.1. Model parameterization

The presented model is parameterized based on the commercial 18,650 cylindrical graphite/NCA Li-ion cell. The cell geometrical parameters are measured for a fresh cell in our laboratory and accepted without modifications. The open circuit potentials (OCVs) for both electrodes are measured at 25 °C in half cells using lithium metal as counter electrode. The parameters of diffusion coefficient of Li ion in separator and in electrode particles and ionic conductivity are taken from similar literature.

The nominal measured capacity is rated as 3.05 [Ah] experimentally during a 1C-rate discharge at 25 °C for this battery. The maximum Li concentration and the porosity values for each electrode are estimated based on the nominal capacity. The maximum Li concentration in the electrodes was calculated from $c_{s,max} = \rho_{theo}/M$, where ρ_{theo} and M are density and the molecular weight of the active solid material, respectively. The volume fraction of active material ε_{active} can then be calculated from Eq. (21), as the transferred capacity (ΔQ).

$$\Delta Q = \Delta c_s V_e \varepsilon_{active} F \tag{21}$$

Here, it is assumed that the solid volume that is not contributing to the nominal capacity of the cell is inactive. Δc_s is the difference between the initial Li concentration $c_{s,0}$ and Li concentration at the end of full-charge, $c_{s,max}$. V_e and F are the effective volume of each electrode and Faraday constants, respectively.

The parameterization of electrochemical and ageing are studied in two steps: (i) determining the electrochemical parameters, such as exchange current density, active material particle radius based on the fresh cell by turning of the ageing reactions (ii) determination of ageing parameters based on the capacity measurement experimental tests.

2.2. Model calibration and validation

2.2.1. Electrochemical parameterization and performance validation

The electrochemical parameterization study is carried out based on the C/3 charge and 1C discharge cycling experimental measurements as shown in Fig. 2a. The cell is discharged from a fully occupied anode (4.2 [V]) to fully unoccupied (2.5[V]). The parameters of exchange current density and the active material particle radius are fitted to experimental 1C cycling data as shown in Fig. 2a by using the method of least squares and the Levenberg-Marquardt (LM) optimization solver. The 1C

Table 4
Governing equations and boundary conditions for separator.

Governing Equations	Boundary Conditions
Mass balance in the separator	
$\frac{\partial c_e}{\partial t} = D_e\frac{\partial^2 c_e}{\partial x^2} + (1-t_+^0)j_{int}$ With initial condition of $c_e\|_{t=0} = c_0$	$-D_{eff,n}\frac{\partial c_e}{\partial x}\|_{x=L_{n^-}} = -D_s\frac{\partial c_e}{\partial x}\|_{x=L_{n^+}}$ $-D_s\frac{\partial c_e}{\partial x}\|_{x=L_{n^-}+L_s} = -D_{eff,p}\frac{\partial c_e}{\partial x}\|_{x=L_{n^+}+L_s}$
Electric potential distribution in separator	
$\nabla\left(-\kappa_{eff}\frac{\partial\varphi_e}{\partial x} + \frac{2\kappa_{sep}RT}{F}(1-t_+^0)\frac{\partial(\ln c_e)}{\partial x}\right) = 0$	$-\kappa_{eff,n}\frac{\partial\varphi_s}{\partial x}\|_{x=L_{n^-}} = -\kappa_{sep}\frac{\partial\varphi_e}{\partial x}\|_{x=L_{n^+}}$ $-\kappa_{sep}\frac{\partial\varphi_e}{\partial x}\|_{x=L_{n^-}+L_s} = -\kappa_{eff,p}\frac{\partial\varphi_s}{\partial x}\|_{x=L_{n^+}+L_s}$

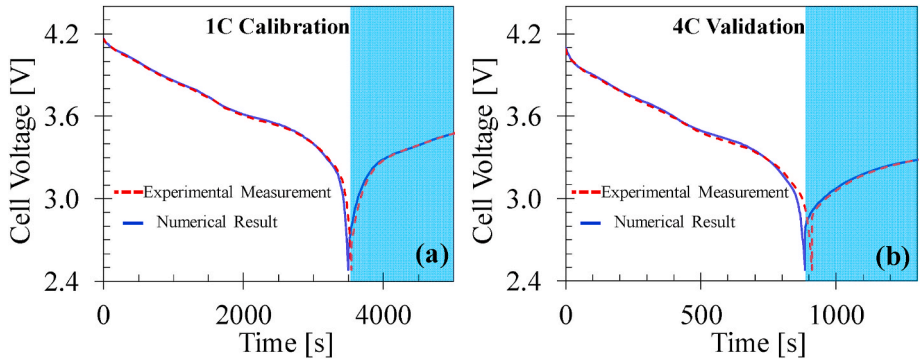

Fig. 2. (a) Comparison of electrochemical model calibration with experimental data in terms of charge/discharge curves at 1C-rate measured for a fresh cell at 25 °C. (b) Model validation using the parameters evaluated from Fig. 2a with experimental data in terms of charge/discharge curves at 4C-rate for a fresh cell at 25 °C.

calibration figure (Fig. 2a) illustrates a good agreement between the model (blue solid-line) and experimental measurements (red dashed-line) for discharging (1C) and C/3 charging (blue region) with an overall root-mean-square error (RMSE) of 1.23%. Then the fitted parameters (listed in Table 1) are used to validate a C/3 charge and 4C discharge electrochemical behaviour. The comparison of discharging (4C) and C/3 charging of the battery again shows quite good agreement with 1.46 [V] % RMSE although the mass and migration of Li ions at higher C-rate noticeably stronger comparing to 1C case. The validation results evidences that the model can capture ionic, electronic, kinetic and diffusion phenomenon accurately for a fresh cell. The fitted parameters here are accepted and kept same without making any modifications.

2.2.2. *Ageing kinetics parameterization and capacity fade - linear and nonlinear ageing*

Capacity loss and resistance increase are the consequence of cell ageing [17,23]. There are many reasons that causes cell ageing, however, the most prominent features are the side reactions, SEI layers and lithium plating that occurs at the anode electrode [8,18,31]. Here we limited the ageing mechanism with the side reactions Eqs. (4), (6) and (7) mentioned in previous section. The ageing parameterization serves vitally important to capture the structural (porosity variation) and chemical features that causes capacity loss. The equilibrium potential of the side reactions Eqs. (4), (6) and (7), volume fractions, and ionic conductivity values are taken from Ref. [31]. However, the kinetic rate constant, diffusion coefficient, molar weight, and density for the EC and DMC compounds are fitted to experimental measured cycling (1C discharge, C/3 charging) data at 25 °C that completed 420 cycles reaching EoL. The fitting is performed via the method of least squares and the LM optimization solver for the 420 cycles (see Table 2 for the ageing parameters).

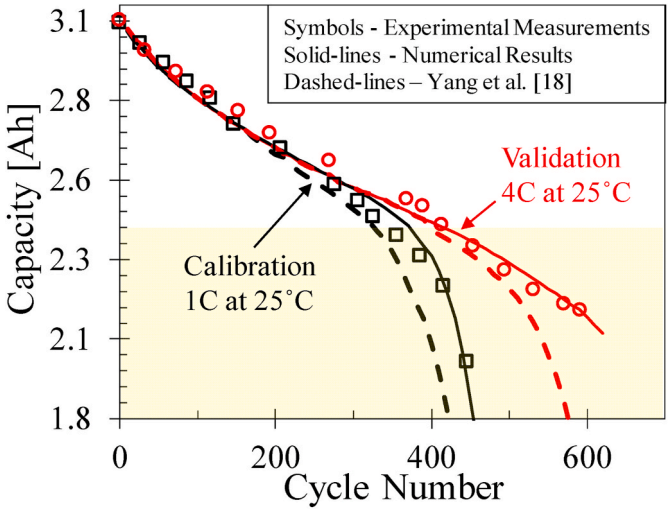

Fig. 3. Comparison of calibrated model (black solid-line) with parameters listed in Table [1,2] against experimental data (square symbols) in constant-current cycling process of 1C discharge and C/3 charge and validated the model (red solid-line) using the same parameter set at 4C discharge and C/3 charge constant current cycling process and compared against experimental measurements at 25 °C. Our model performance is also compared against Yang et al.'s ageing model [18] (black dashed-line).

The capacity degradation as a function of the cycle number using the optimized parameters is plotted to show the comparison of the fitted model results (black solid-line) against experimental measured data (black square symbols) in Fig. 3. The model results match fairly well with a goodness-of-fit-error (GoF) of 98.76%, indicating that the model is able to predict the internal cell characteristics (structural modification and chemical features) reliably throughout the lifespan of the cell and can simulate nonlinear capacity fade. The nominal capacity drop of 15.96% after 300 cycles in Fig. 3 is attributed to the active material loss and electrolyte consumption loss caused by the side reactions [7,18,21,31]. Moreover, after the 300th cycle the cell lost 32% of capacity in 160 cycles. This sudden capacity loss (nonlinear ageing or knee-point) is due to severe deterioration of ion kinetics and local porosity clogging at the anode/separator interface as depicted in Fig. S2 (b). This clogging likely increases the over potential for lithium-ion transport in the anode electrode and may lead to nonlinear capacity fade and lithium-plating at moderate temperatures and charging steps as explained previously by Ref. [8,15,32].

Using the optimized parameters (based on the C/3 charging - 1C discharging cycling) the model is used to predict and validate the nominal capacity fade for the 4C discharge and C/3 charging constant current cycling. Fig. 3 shows the nominal capacity fade as a function of cycle number for the 4C discharge and C/3 charging constant current cycling. Interestingly, both the model and the measured data shows almost a linear capacity fade until 600 cycles. The results show that the ageing model can maintain sufficient accuracy in terms of capacity degradation response prediction with a GoF of 98.17%. In comparison to the 1C discharging, 4C discharging shows higher lifetime without showing a transition from linear to nonlinear. As can be seen in Fig. S3 (a), the contribution of the plating is only 5% to total capacity loss, whereas the SEI growth due to the EC reduction hits to around 70% with remarkable amount of DMC reduction, 25%. It worth to note that because of the EC denser structure, the capacity retention is quite large although Li-plating is not observed significantly. This behaviour qualitatively agrees with the results from Ref. [15,16]. Also, the capacity degradation after 200 cycles show linear behaviour, this characteristic is purely due to EC component of SEI growth as depicted in Fig. S2 (a). The yellow region in Fig. 3 is the 80% threshold of the initial capacity, which is typically considered as the EoL for an EV battery.

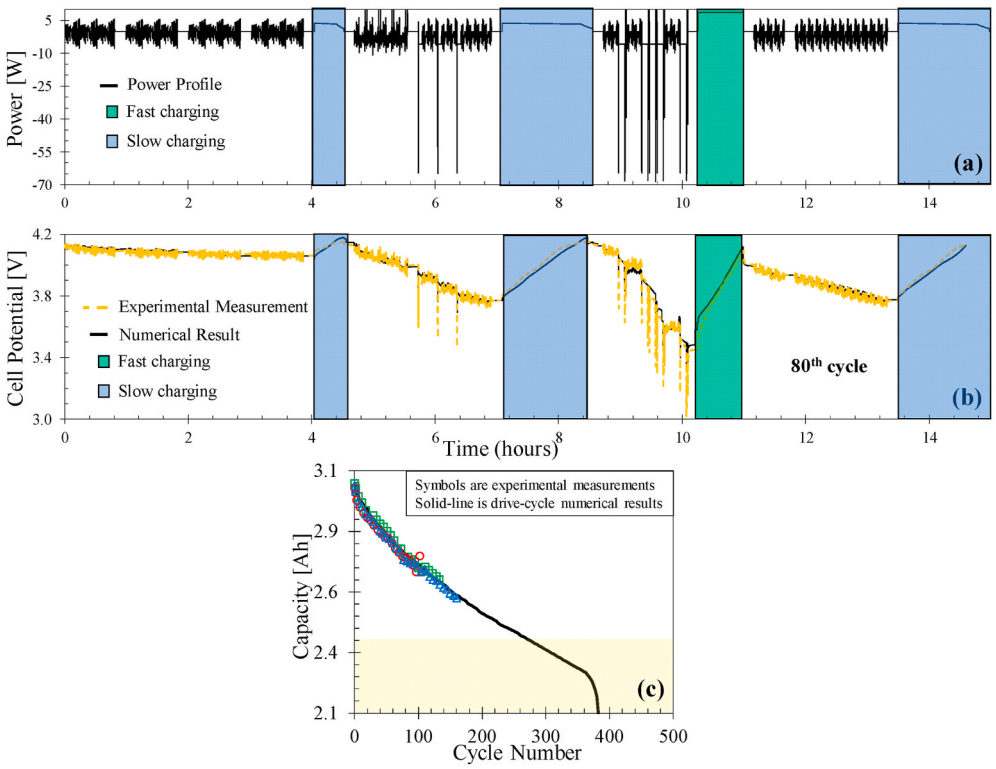

Fig. 4. (a) Power-profile used in weekly driving includes conventional CC/CV slow (blue zone) and fast (green zone) charging. (b) Model validation simulation results (black solid-line) with 80th cycle cell experimental measurement (yellow dashed-line) based on the power profile input. (c) Capacity loss observed in drive-cycle ageing campaign at 25 °C (symbols) and lifetime prediction of the cell by numerical results (solid-line).

Furthermore, we compared our experimental results against existing ageing models in Ref. [18] using the optimized parameters in Table 2. The discrepancy of the present model with the aforementioned study can be explained as follows: (i) The growth of SEI is assumed to be induced due to the diffusion of electrolyte solvent only across the surface film, which is not practical given the reality of electrolyte solvent mass transport; (ii) The ageing mechanism in the present study is modelled by two electrochemical side reactions by including the effect of EC and DMC electrolyte solvents. While Refs. [17,18,23] included the effects of only EC with a fixed EC diffusion coefficient, whereas the EC diffusion coefficient in this work varies with porosity in time and anode electrode thickness [7]; (iii) In this work, the contributions of the $(CH_2OCO_2Li)_2$, Li_2CO_3 solvent products and lithium deposition amount are considered for surface film resistance calculation, however, Li_2CO_3 contribution is only assumed in Ref. [17,18]. This simplification causes inaccurate local porosity calculation, which is not ideal as one of the main reasons causing nonlinear capacity fade is the sudden local porosity clogging; (iv) The ionic conductivity is a dependent parameter of the products deposited on the active material surface and also local porosity. Therefore, these assumptions bring about the improvement in the results. We expect that our findings will play a key role in the design of better performance and longer life batteries or cells. Details of ageing mechanisms and its contributions to anode porosity change is provided in the Supplement Information Section.

2.2.3. *Life-time prediction of an EV cell under real-life scenario*

Using the validated ageing parameters from Section 4.2.2 the next validation step includes the emulation of a real-life scenario with a dynamic power profile, Fig. 4a, that represents a one-week driving-cycle. One week of driving includes a sequence of working-days and performance driving with the feature of regenerative trips, and slow (blue marked)/fast (green marked) charge from the grid. This kind of scenario assists the lifetime prediction of the cell under a real operation condition.

Fig. 4b first shows the numerical result for voltage validation for the 80th power profile cycle under 25 °C. The objective of this validation is to evaluate the model prediction accuracy for combined driving events and slow/fast charging procedures effects on the voltage curve for an aged cell. The presented model is able to predict the cell voltage response (for the 80th power profile cycle) with 98.54% of GoF. In view of this results, the developed electrochemical model can simulate the dynamic power profile despite the highest current peak reaches 6C rate and includes fast-charging mechanism.

Fig. 4c reveals the validation for the nominal capacity loss of the numerical results compared against experimental measurement data for three cells tested under the dynamic power profile as a function of cycle number. The model was used to forecast the future capacity loss of the cells.

Up until the (~160 cycles) the model demonstrates a near linear capacity fade with a good agreement to the measured data (98.42 of GoF). Beyond the 50 cycles the model continued to predict a near linear fade and predicts an EoL of 294 cycles to reach 80% of initial capacity (indicated by the yellow region in Fig. 4c). As the simulation continues the model demonstrates that around the 370th cycle the nonlinear degradation occurs. These results are significant as they demonstrate how a physics-based ageing model parameterized for CC cycling can validate and forecast battery ageing for a dynamic power profile with nonlinear capacity fade.

3. Conclusion

In this paper, we introduced a novel ageing mechanism that extends the common approach of transport limited models by incorporating (i) multi-layered SEI, (ii) lithium-plating, (iii) reduction of anode porosity. By this approach, we aimed to a gain a fundamental understanding for linear and nonlinear capacity fade by modelling more realistic ageing

kinetics. The model is calibrated and validated against both fresh and aged NCA/graphite commercial cell through a series of experiments including (i) constant-current cycling and (ii) dynamic power profile conditions at ambient temperature of 25 °C. The parameters used in the model are experimentally measured and optimized based on the fresh and aged cell (for a C/3 charging – 1C discharging CC profile). The model subsequently predicts the linear and nonlinear capacity fades for a different (C/3 charging - 4C discharging) CC cycling data with 98% of GoF and predicts better than existing well-accepted ageing models [17, 18,22,23]. Moreover, for the first time we validated the terminal voltage response and capacity fade based on a dynamic power profile with a 98.54% and 98.42% GoFs, respectively. Quantifying all these degradation processes precisely will improve lifetime prediction of cell capacity during cell operation. This model will allow us to better predict the lifetime of a Li-ion battery under real operating conditions which required a reliable integration of the battery into an EV application and for warranty evaluations.

CRediT authorship contribution statement

Selcuk Atalay: Conceptualization, Writing - review & editing, Writing - original draft, Methodology, Software, Validation, Investigation, Data curation, Formal analysis, contributed to conceptualization, mathematical modelling, writing the original draft with supporting information, and its reviewing and editing. **Muhammad Sheikh:** Writing - review & editing, performed the cell testing and wrote the experimental part. **Alessandro Mariani:** (former Aston Martin Lagonda and now FPT) supported with the power profile designs . **Yu Merla:** (Williams Advanced Engineering) supported with the power profile designs and together with . **Ed Bower:** (AML) supported the discussions of the results, (AML) supported the discussions of the results, (AML) supported the discussions of the results. **W. Dhammika Widanage:** Writing - review & editing, Widanage reviewed and edited the draft and leaded the project in WMG.

Declaration of competing interest

The authors declare that they have no known competing financial interests or personal relationships that could have appeared to influence the work reported in this paper.

Acknowledgement

This work was supported by Catapult 8205 and IUK H1PERBAT Grants. The authors also would like to thank to Dr. Muhammad Rashid, Research Fellow at WMG, University of Warwick, for fabricating a half cells from fresh commercial cells and measuring the open circuit potential for anode and cathode materials.

Appendix A. Supplementary data

Supplementary data to this article can be found online at https://doi.org/10.1016/j.jpowsour.2020.229026.

References

[1] B. Scrosati, J. Garche, J. Power Sources 195 (2010) 2419–2430.
[2] Z.P. Cano, D. Banham, S. Ye, A. Hintennach, J. Lu, M. Fowler, Z. Chen, Nat. Energy 3 (2018) 279–289.
[3] A.S. Mussa, A. Liivat, F. Marzano, M. Klett, B. Philippe, C. Tengstedt, G. Lindbergh, K. Edström, R.W. Lindström, P. Svens, J. Power Sources 422 (2019) 175–184.
[4] Y. Liu, Y. Zhu, Y. Cui, Nature Energy 4 (2019) 540–550.
[5] J. Vetter, P. Novák, M.R. Wagner, C. Veit, K.-C. Möller, J. Besenhard, M. Winter, M. Wohlfahrt-Mehrens, C. Vogler, A. Hammouche, J. Power Sources 147 (2005) 269–281.
[6] M. Ecker, N. Nieto, S. Käbitz, J. Schmalstieg, H. Blanke, A. Warnecke, D.U. Sauer, J. Power Sources 248 (2014) 839–851.
[7] W. Huang, P.M. Attia, H. Wang, S.E. Renfrew, N. Jin, S. Das, Z. Zhang, D.T. Boyle, Y. Li, M.Z. Bazant, Nano Lett. 19 (2019) 5140–5148.
[8] X.-G. Yang, T. Liu, Y. Gao, S. Ge, Y. Leng, D. Wang, C.-Y. Wang, Joule 3 (2019) 3002–3019.
[9] K.P. Yao, J.S. Okasinski, K. Kalaga, I.A. Shkrob, D.P. Abraham, Energy Environ. Sci. 12 (2019) 656–665.
[10] X. Zhang, Y. Gao, B. Guo, C. Zhu, X. Zhou, L. Wang, J. Cao, Electrochim. Acta (2020) 136070.
[11] J. Pu, J. Li, Z. Shen, C. Zhong, J. Liu, H. Ma, J. Zhu, H. Zhang, P.V. Braun, Adv. Funct. Mater. 28 (2018) 1804133.
[12] J. Zhu, M.S.D. Darma, M. Knapp, D.R. Sørensen, M. Heere, Q. Fang, X. Wang, H. Dai, L. Mereacre, A. Senyshyn, J. Power Sources 448 (2020) 227575.
[13] P. Guan, L. Liu, X. Lin, J. Electrochem. Soc. 162 (2015) A1798–A1808.
[14] S. Bourlot, P. Blanchard, S. Robert, J. Power Sources 196 (2011) 6841–6846.
[15] S.F. Schuster, T. Bach, E. Fleder, J. Müller, M. Brand, G. Sextl, A. Jossen, J. Energy Storage 1 (2015) 44–53.
[16] T.C. Bach, S.F. Schuster, E. Fleder, J. Müller, M.J. Brand, H. Lorrmann, A. Jossen, G. Sextl, J. Energy Storage 5 (2016) 212–223.
[17] M.B. Pinson, M.Z. Bazant, J. Electrochem. Soc. 160 (2013) A243–A250.
[18] X.-G. Yang, Y. Leng, G. Zhang, S. Ge, C.-Y. Wang, J. Power Sources 360 (2017) 28–40.
[19] J.M. Reniers, G. Mulder, D.A. Howey, J. Electrochem. Soc. 166 (2019) A3189.
[20] P. Lu, C. Li, E.W. Schneider, S.J. Harris, J. Phys. Chem. C 118 (2014) 896–903.
[21] H. Ge, T. Aoki, N. Ikeda, S. Suga, T. Isobe, Z. Li, Y. Tabuchi, J. Zhang, J. Electrochem. Soc. 164 (2017) A1050–A1060.
[22] S. Das, P.M. Attia, W.C. Chueh, M.Z. Bazant, J. Electrochem. Soc. 166 (2019) E107–E118.
[23] H. Ekström, G. Lindbergh, J. Electrochem. Soc. 162 (2015) A1003–A1007.
[24] L.L. Lam, R.B. Darling, J. Power Sources 276 (2015) 195–202.
[25] X. Lin, J. Park, L. Liu, Y. Lee, A. Sastry, W. Lu, J. Electrochem. Soc. 160 (2013) A1701–A1710.
[26] M. Safari, M. Morcrette, A. Teyssot, C. Delacourt, J. Electrochem. Soc. 156 (2009) A145–A153.
[27] P. Lu, S.J. Harris, Electrochem. Commun. 13 (2011) 1035–1037.
[28] P.M. Kekenes-Huskey, C.E. Scott, S. Atalay, J. Phys. Chem. B 120 (2016) 8696–8706.
[29] J. Newman, K.E. Thomas-Alyea, Electrochemical Systems, John Wiley & Sons, 2012.
[30] F. Single, B. Horstmann, A. Latz, Phys. Chem. Chem. Phys. 18 (2016) 17810–17814.
[31] N. Paul, J. Keil, F.M. Kindermann, S. Schebesta, O. Dolotko, M.J. Mühlbauer, L. Kraft, S.V. Erhard, A. Jossen, R. Gilles, Journal of Energy Storage 17 (2018) 383–394.
[32] G. Sikha, B.N. Popov, R.E. White, J. Electrochem. Soc. 151 (2004) A1104–A1114.